Nanoscale Research Letters

RESEARCH

Open Access

Multi-level Cells and Quantized Conductance Characteristics of Al_2O_3-Based RRAM Device for Neuromorphic System

Yunseok Lee[1], Jongmin Park[1], Daewon Chung[1], Kisong Lee[2] and Sungjun Kim[1*]

Abstract

Recently, various resistance-based memory devices are being studied to replace charge-based memory devices to satisfy high-performance memory requirements. Resistance random access memory (RRAM) shows superior performances such as fast switching speed, structural scalability, and long retention. This work presented the different filament control by the DC voltages and verified its characteristics as a synaptic device by pulse measurement. Firstly, two current–voltage (*I–V*) curves are characterized by controlling a range of DC voltages. The retention and endurance for each different *I–V* curve were measured to prove the reliability of the RRAM device. The detailed voltage manipulation confirmed the characteristics of multi-level cell (MLC) and conductance quantization. Lastly, synaptic functions such as potentiation and depression, paired-pulse depression, excitatory post-synaptic current, and spike-timing-dependent plasticity were verified. Collectively, we concluded that Pt/Al_2O_3/TaN is appropriate for the neuromorphic device.

Keywords: Neuromorphic system, Memristor, Al_2O_3, Quantized conductance, MLC

Introduction

In an environment where data demand is rapidly increasing, a breakthrough is needed in computing performance limitations due to serial processing of CPU and memory [1]. It is necessary to change the computing structure and improve the materials of the memory device to solve the memory wall. Neuromorphic computing architecture is emerging as a structural solution to the bottleneck. The neuromorphic computing system mimics the neuron and synapses of the human brain [2–4]. This system is suitable for the process of complex and unstructured information. First of all, to implement neuromorphic computing, it is necessary to understand how the human brain processes information. The human brain includes numerous synapses and neurons, and learning and memory of information proceed through parallel chemical interactions. Information processing and memory capabilities vary depending on various factors such as the size, holding time, and a repetition time of external signals and stimuli [5–7].

Among various memories, the RRAM exhibits a fast switching speed and a low operating voltage [8–15]. In addition, RRAM could be implemented in a simple structure such as a metal-oxide-metal (MIM) with various structural expandability [16–21] such as the connection of transistor with each memory cell, an array structure, and a 3D vertical structure.

The switching of RRAM occurs by the formation and rupture of filament in an insulator between the metals [22–26]. The resistance of RRAM is varied through a conductive filament composed of oxygen vacancy in the insulator existing between the top electrode (TE) and bottom electrode (BE) and has two basic switching states (high and low) to process the data storage process [20, 27–30]. In the case of the high-resistance state

*Correspondence: sungjun@dongguk.edu

[1] Division of Electronics and Electrical Engineering, Dongguk University, Seoul 04620, Republic of Korea
Full list of author information is available at the end of the article

(HRS), a low current flows in HRS, and in the case of the low-resistance state (LRS), it means a state has low resistance and good conductivity. Accordingly, the on/off state could be monitored through the read voltage. The repetition of set and reset processes cause the device to move back and forth between the HRS and LRS, which can be described as a memory that stores 0 and 1 from a digital perspective.

In this paper, the gradual resistive switching is conducted on Pt/Al_2O_3/TaN device, including Al_2O_3 high-k dielectric [31–35], which was deposited by atomic layer deposition (ALD) equipment. The characteristics using basic DC current sweep and on/off endurance characteristics were measured, and the suitability of neuromorphic devices was also measured through synaptic measurement, including potentiation, depression, PPD, EPSC, and STDP.

Experiments

Pt/Al_2O_3/TaN device was fabricated as follows. Firstly, TaN as BE was deposited by the sputtering system on SiO_2/Si wafer. A 5-nm-thick Al_2O_3 film was deposited by the ALD process. In the ALD process, TMA precursors and O_3 were used at stage temperature 450 °C. Then a 100-nm-thick Pt as TE was deposited by evaporator in which the top pattern was formed in a circular pattern by using a shadow mask with a diameter of 100 µm. For the measurement environment, all measurements were performed at room temperature and ambient atomic pressure. Electrical data were measured using the Keithley 4200-SCS semiconductor parameter ultrafast module and in pulse mode using a 4225-PMU ultrafast module.

Results and Discussion

Figure 1a shows the schematic illustration of the fabricated Pt/Al_2O_3/TaN device. In Fig. 1b, the cross section of the Pt/Al_2O_3/TaN RRAM device is inspected by a transmission electron microscope (TEM). The thickness of the Al_2O_3 insulator layer deposited by the ALD system is about 5 nm. In Fig. 1c, energy dispersion X-ray spectroscopy (EDS) mapping of each element was performed to investigate possible chemical interactions. EDS mapping shows the spatial distribution of elements in Pt/Al_2O_3/TaN. EDS maps of Pt, Al, O, Ta, and N elements were collected in the area shown in the electronic image. A region where O and Ta overlap is observed, indicating The TaON interface layer between the Al_2O_3 insulator and TaN BE is formed by a chemical redox reaction between the TaN BE and the lower Al_2O_3 layer due to the strong oxygen binding of TaN [36–38]. Because of the formation of the TaON interface layer by extracting oxygen from the Al_2O_3 layer by TaN, better switching characteristics could be exhibited according to the formation of the oxygen vacancy near the TaON/Al_2O_3 interface [38].

In order to confirm the TaON layer, the X-ray photoelectron spectroscopy (XPS) spectra fittings were conducted. Figure 2a shows the Al 2*p* XPS spectra in which peak intensity is located at 75 eV for Al–O bonding [39]. Figure 2b and c shows Ta 4*f* and N 1*s* XPS peak for the TaON layer. In Fig. 2b, small peaks exist at higher binding energy than general Ta 4*f* XPS peaks. This indicates that the binding Ta–O or Ta–Al energy also affected the Ta 4*f* XPS peaks with binding Ta–N energy [40, 41]. From Fig. 2c, through combination with oxygen, N 1*s* XPS peak shows more biased to higher binding energy than the normal N 1*s* peak [42]. As a result, a thin layer of TaON exists between the Al_2O_3 insulator and the TaN BE.

Next, we investigate two types of bipolar resistive switching by DC sweep. All of the above *I–V* characteristics were measured at a step voltage of 0.01 V. Representative feature of this device shows forming-free characteristics in Fig. 3a [43]. The set process has similar *I–V* curves as the forming process, and the set process occurs at −2 V or higher, and the reset process is induced by applying a 2.75 V. This is referred to as a deep reset curve. At this time, the on/off ratio is about 45,000 based on the read voltage of 0.5 V, which is a characteristic due to a large band gap of Al_2O_3. Set shows abrupt behavior, and in the reset process, it shows a curve that returns to the HRS state with a stepwise drop from 1 V or higher to 2.7 V. In the case of Fig. 3b, unlike Fig. 3a, it can be implemented by adjusting reset voltage less than 2.75 V. This is referred to as a partial reset curve, and the on/off ratio at this time is about 13 at the read voltage of 0.5 V. Compared to the *I–V* curves with fully reset, the *I–V* curves with partial reset process shows more gradual characteristics in the set and reset processes. Both *I–V* characteristics have self-compliance characteristics [44]. The method of connecting the two differences in Fig. 3a and b can be confirmed by a continuous DC sweep in Fig. 3c. The deep reset occurs when the larger voltage is applied, indicating that the strength of the reset can be controlled by the voltage adjustment. The current flows in the HRS induced by the partial reset and an additional reset occur, which lowers the current level due to additional filament decomposition. Figure 3d exhibits a possible switching mechanism of partial reset (left) and deep reset (right) curves. As confirmed in Fig. 2, Al–O bonding has higher binding energy than that Ta–O bonding. This suggests that switching depends on the TaON layer when the small electric field is applied and on the Al_2O_3 layer when it is a large electric field. Thus, oxygen ions formed between TaN and TaON affect the conduction mechanism of the device and are estimated to result in MLC characteristics [3, 45, 46]. Gradual partial reset with

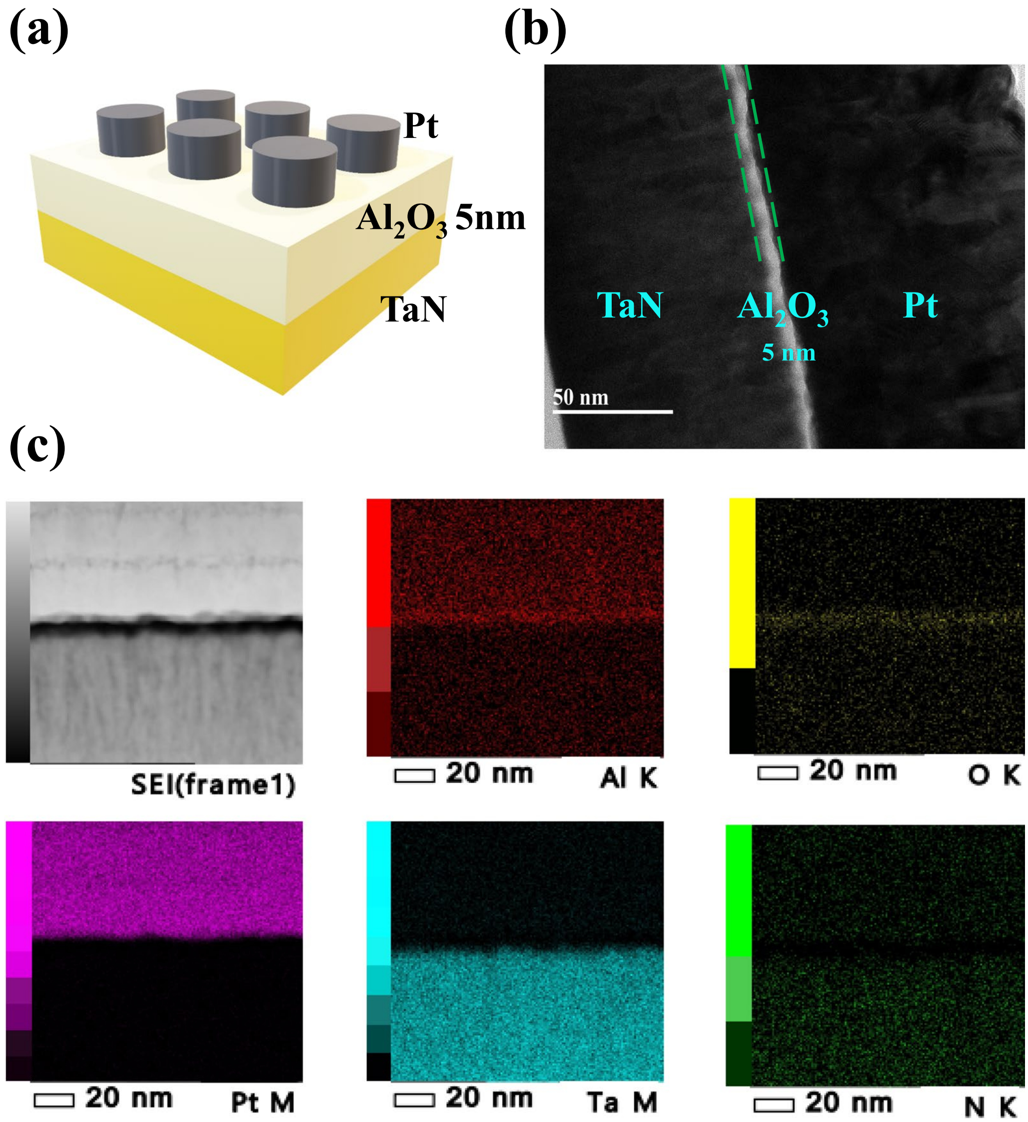

Fig. 1 **a** Schematics image of Pt/Al_2O_3/TaN device, **b** cross-sectional TEM image, **c** EDS mapping images of Pt, Al, O, Ta and N elements collected from the area indicated in the TEM image of the Pt/Al_2O_3/TaN device

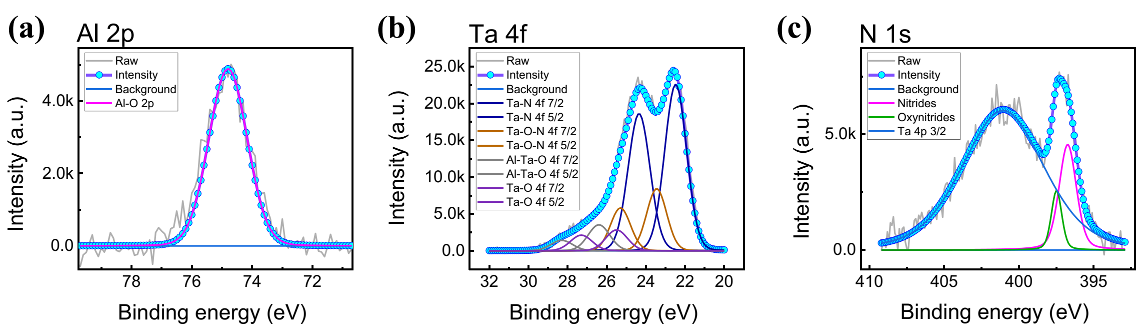

Fig. 2 XPS spectra of **a** Al 2*p*, **b** Ta 4*f* and **c** N 1*s* of the device

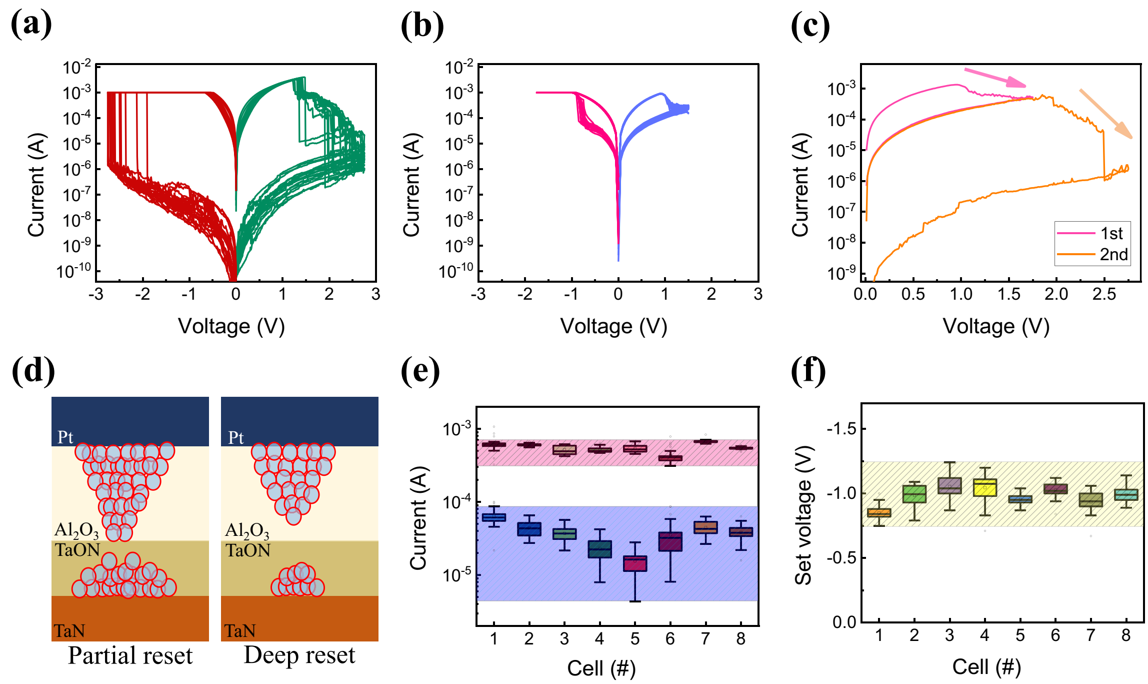

Fig. 3 Bipolar resistive switching of Pt/Al_2O_3/TaN device: **a** deep reset, **b** partial reset, **c** process of inducing from partial reset to deep reset, and **d** deep and partial reset mechanism schematic diagram. Uniformity of **e** HRS and LRS, **f** set voltage

MLC occurs in the TaON layer within the − 2.2 V region. However, the more electric field induces the filament decomposition inside the Al_2O_3 and causes the abrupt current decrease during the reset process. In Fig. 3e, HRS and LRS were confirmed in the read operation of 0.5 V to demonstrate state uniformity. Since the filament decomposition depends on the magnitude of reset voltage, HRS varies more severely than LRS. Also, more decomposition demands more set voltage to re-form the filaments. Variation of set voltage is shown in Fig. 3f and it varied from − 1.25 to − 0.75 V in accordance with the previous reset cycle process.

In Fig. 4a, the endurance characteristics were also measured for partial *I*–*V* conditions using pulse for 10^5 cycles. It shows that HRS and LRS can be switched even at 10^5 or more times. In Fig. 4b, it is the result of performing the retention test for each *I*–*V* characteristic including partial and deep resets. HRS and LRS were measured at the read voltage of 0.15 V, and both states were maintained for 10^4 s. These results show the Pt/Al_2O_3/TaN device has good non-volatile memory properties. Multi-level cell characteristics are very beneficial for practical applications such as high-density memory and neuromorphic device [43, 47, 48]. Figure 4c shows a reset process by increasing the reset voltage by 0.2 V for each cycle. Through this process, as the reset voltage increases, multiple HRS is achieved. In Fig. 4d, based on the reset voltage at the boundary between the partial reset and deep reset, the reset process was repeatedly measured while increasing 0.025 V from 1.8 to 2.35 V. It could be verified that the current level gradually decreases, and this could prove the existence of various multi-level states.

The property of conductance quantization [49–52] was confirmed. This is thought to be due to the quantization effect of conductive filament during the reset process. When the conductive filament is well controlled, it is possible to implement more state and higher density memory through this phenomenon. As shown in Fig. 5a, this phenomenon can be observed when the conductive filament is modified in atomic units. The step voltage of 0.002 V and delay time of 0.3 s every step is used to observe quantization in multiple cycles, and only elemental disruption of the filament was measured during the reset process. The conductance quantum, represented by the symbol G_0, is the quantized unit of electrical conductance. It is defined by the elementary charge e and Planck constant h as $G_0 = 2e^2/h = 7.74809 \times 10^{-5}$ S. The device takes an integer multiple of G_0 or an intermediate value between integers. In the end, LRS is changed to HRS. The statistical analysis is essential through multiple cycles [53–57]. Figure 5b shows the histogram plotting, and it can be seen that even in various conductance steps, there is a high tendency near a multiple of G_0 or

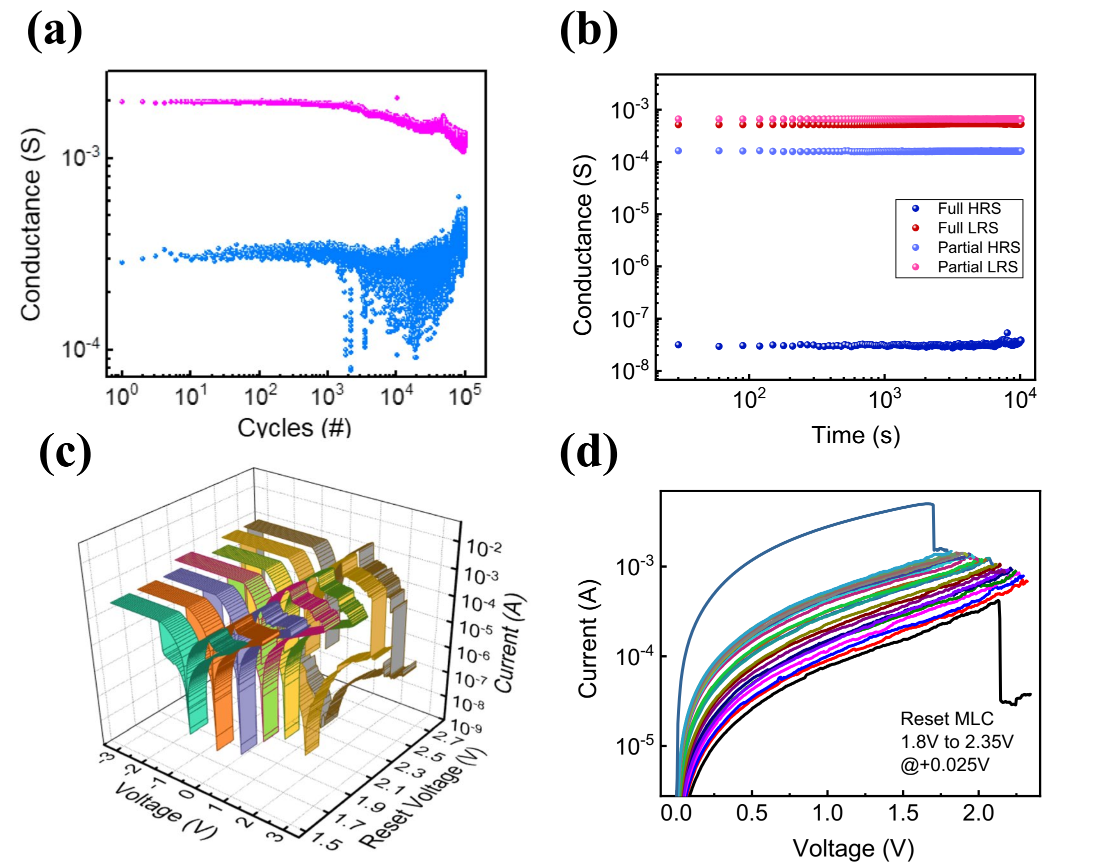

Fig. 4 **a** Endurance characteristic of the device for 10^5 cycles and **b** each deep and partial HRS and LRS retention characteristics for 10^4 s. MLC characteristics of **c** different reset voltages, **d** consecutive incremental voltage repetition

a half multiple [58–61]. It is noted the values between $0.5G_0$ and $3G_0$ are distinctly distinguishable. It may be necessary to make the conducting filament smaller by means of a method such as making the device smaller in order to distinguish the quantized values. Pulse measurements were performed in Fig. 5c and d to describe the quantized conductance [62–64]. Conductance calculated with the voltage of 0.5 V was induced by adding write pulses at 0.5 s intervals. In Fig. 5c, an incremental write pulse increased by −25 mV from −0.7 to −1.775 V was used and the abrupt set operation occurred at a voltage of −1 V or higher. The conductance in HRS increases more than $10G_0$ at a time due to the abrupt characteristic in the set region. This characteristic was also confirmed in the *I–V* curve in the inset image of Fig. 5c, which MLC implemented by limiting compliance current. In contrast, conductance quantization with the erase pulses composed by 25 mV from 1.5 to 2.175 V were ranged of about G_0. From those two different conductance ranges show that it is more ease to implement MLC during reset process due to the clear state distinction.

A neuromorphic computing system can be implemented using multi-level cells in Pt/Al_2O_3/TaN devices. As shown in Fig. 6a, the conductive filament connecting the TE and BE of RRAM can be expressed very similarly to the human's biological system [43, 65–67]. In order to confirm the suitability of neuromorphic computing, pulse measurements were conducted. In Fig. 6b, conductance control is continuously performed through 5 cycles of potentiation and depression by applying the pulses. Potentiation and depression were set to −1.15 V and 1.3 V, respectively, and both pulse widths were set to 10 sμ. From the *I–V* characteristic of the set process, relatively abruptness in the potentiation can be confirmed. It could be verified that the depression part has a more gradual characteristic. Moreover, we demonstrate more gradual and symmetric resistance-change characteristics by controlling the voltage amplitude of pulses in Fig. 6c [68, 69]. Each 6 potentiation and depression segments are used to increase and decrease the conductance. The voltage varied from −0.9 to −1.4 V for potentiation and from

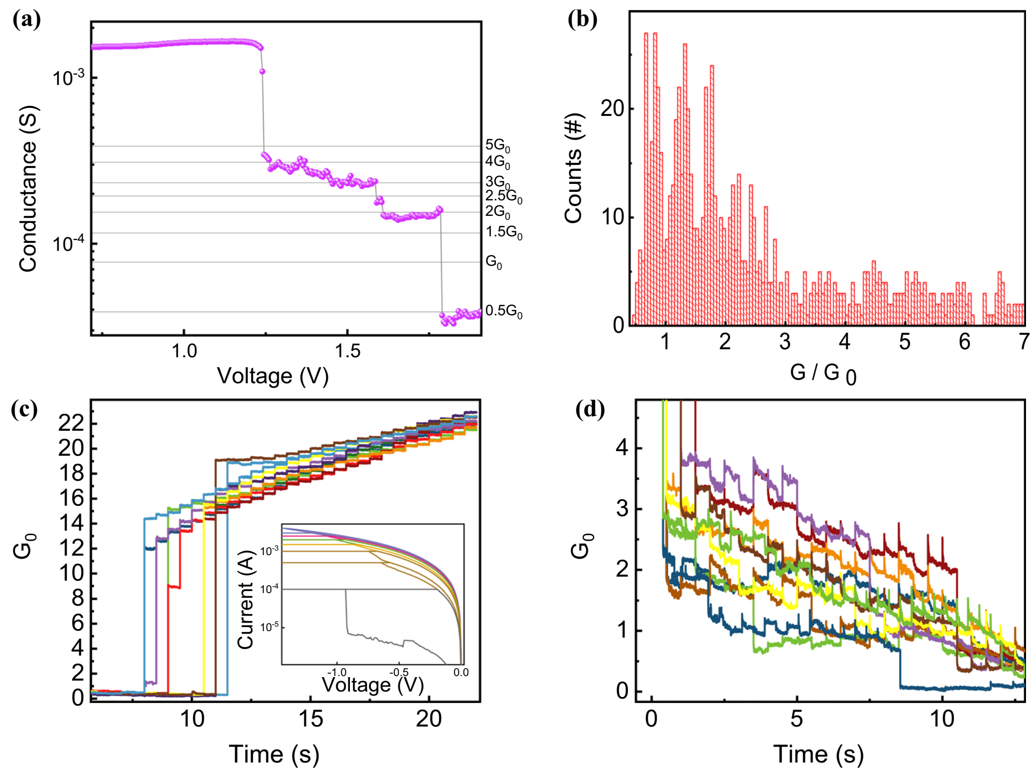

Fig. 5 **a** Quantized conductance characteristic using DC measurement on reset part, and **b** histogram of quantized conductance levels. Quantized conductance characteristic using pulse measurement **c** in set region, **d** in reset region

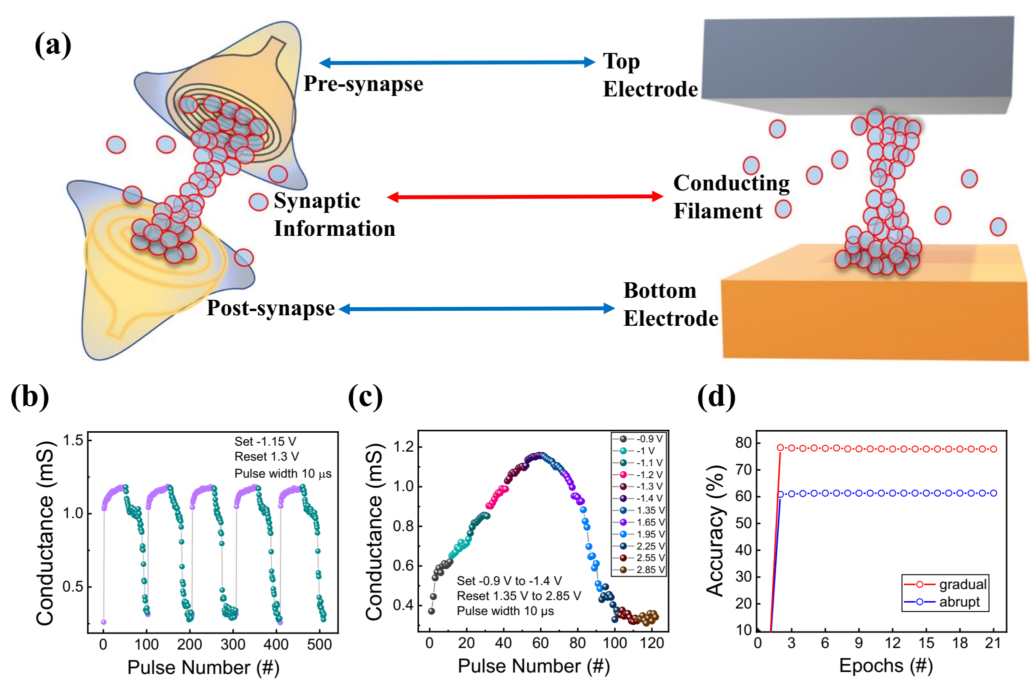

Fig. 6 **a** Schematic illustration of similarity between human synaptic neural structure and RRAM device structure. Potentiation and depression characteristics: **b** consecutive same voltage pulse, **c** single incremental voltage pulse. **d** MNIST pattern recognition simulation results of (**b**) and (**c**)

1.35 to 2.85 V for depression. Figure 6d shows MNIST pattern recognition simulation results by using the conductance results of Fig. 6b and c [70, 71]. The result of using Fig. 6c shows higher accuracy for each epoch. In other words, pulse improvement measurement provides a better learning process.

Synaptic functions, such as PPD, EPSC, and STDP measurements, were performed to determine suitability for the neuromorphic application [72–74]. Figure 7a shows the device's PPD measurement data, the ratio change between two pulses was confirmed when the seven different intervals were used. Synaptic weight changed with the time interval ranging from 20 µs to 5 ms between two consecutive depression pulses. The amount of synaptic weight change was expressed as $\Delta W = (A_2 - A_1)/A_1 \times 100$ (%). As a result, the current responded by the second pulse decreases as the interval increases, indicating that the device is suitable for implementing STP. Figure 7b illustrates conductance changes before and after giving five identical write pulses and summarizes them with pulse amplitudes. As the voltage amplitude increases, both potentiation and depression have a larger synaptic weight change. Continuous stimulation raises EPSC; the degree of weight strengthening can be adjusted according to the amplitude. The strength of connections between neurons in biological synapses can be controlled by STDP. Therefore, if we can elucidate the detailed mechanisms of biological synaptic action and imitate the action behavior, it will be possible to mimic the energy-efficient processing of the human brain. Figure 7c explains the configuration of the STDP protocol. When the pre-spike signal and post-spike signal, which vary with the interval, were applied to the biological synapses, the weight was changed and implemented

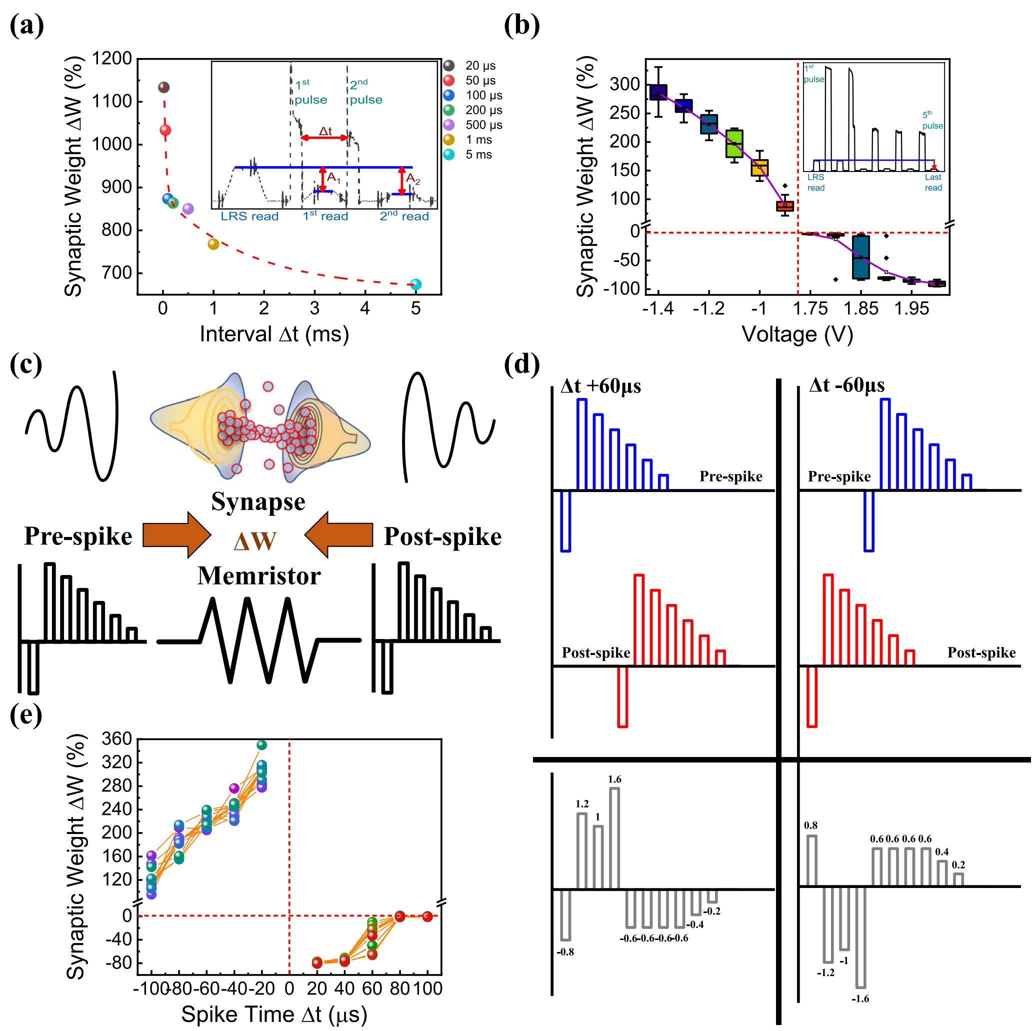

Fig. 7 **a** PPD measurement, **b** EPSC data according to amplitude. STDP characteristics: **c** Schematic for measurement imitation between synaptic neural structure and RRAM, **d** pulse authorization for STDP measurement at $\Delta t = 60$ µs and **e** result of STDP measurement

according to the learning behavior. This process was mimicked on the memristor in the same way. The pulse protocol in Fig. 7d was used for the measurements. The same pre and post-signal were composed, but the different shape of pulses was finally configured and applied according to the interval. Since the final pulse configuration was different, the synaptic weights over time had different weight changes, as shown in Fig. 7e [2, 75, 76]. In general, the shorter the absolute time of the spike time difference, the greater the change in conductance change like a biological synapse.

Conclusions

As a result, the MLC characteristics and quantized conductance were confirmed through the Al_2O_3-based RRAM device deposited with ALD, and excellent biological characteristics were investigated through pulse measurement. DC I–V bipolar switching characteristics were verified through DC measurement, and it was verified that switching characteristics of two different characteristics could be easily controlled only by adjusting a voltage. Multi-levels in various cases were confirmed by varying the amount of voltage that adjusts different characteristics, and the conductance quantization phenomenon was also confirmed within the reset section and pulse measurements. This MLC phenomenon was connected with pulse measurement to measure potentiation and depression, and it was possible to maximize MLC characteristics through voltage control of each segment. Including PPD and EPSC, through the measurement of STDP, the change in the conductance weight of the device was confirmed by imitating the synapse. In conclusion, the MLC characteristics of the device and the suitability of neuromorphic computing were successfully completed.

Acknowledgements
Not applicable.

Author Contributions
All authors read and approved the final manuscript.

Funding
This research was supported in part by National R&D Program through the National Research Foundation of Korea (NRF) funded by Ministry of Science and ICT (2021K1A3A1A49098073) and in part by Korea Institute of Energy Technology Evaluation and Planning (KETEP) grant funded by the Korea Government (MOTIE) under Grant 20224000000020.

Availability of Data and Materials
All data generated or analysed during this study are included in this article.

Declarations

Ethics Approval and Consent to Participate
Not applicable.

Consent for Publication
Not applicable.

Competing interests
The authors declare they have no competing interests.

Author details
[1]Division of Electronics and Electrical Engineering, Dongguk University, Seoul 04620, Republic of Korea. [2]Department of Information and Communication Engineering, Dongguk University, Seoul 04620, Republic of Korea.

Received: 26 June 2022 Accepted: 24 August 2022
Published online: 03 September 2022

References

1. Wang R, Yang J-Q, Mao J-Y et al (2020) Recent advances of volatile memristors: devices, mechanisms, and applications. Adv Intell Syst. https://doi.org/10.1002/aisy.202000055
2. Kim S, Kim H, Hwang S et al (2017) Analog synaptic behavior of a silicon nitride memristor. ACS Appl Mater Interfaces 9:40420–40427. https://doi.org/10.1021/acsami.7b11191
3. Ismail M, Abbas H, Sokolov A et al (2021) Emulating synaptic plasticity and resistive switching characteristics through amorphous Ta_2O_5 embedded layer for neuromorphic computing. Ceram Int 47:30764–30776. https://doi.org/10.1016/j.ceramint.2021.07.257
4. Li Q, Tao Q, Chen Y et al (2021) Low voltage and robust InSe memristor using van der Waals electrodes integration. Int J Extreme Manuf. https://doi.org/10.1088/2631-7990/ac2296
5. Ryu H, Kim S (2020) Self-rectifying resistive switching and short-term memory characteristics in Pt/HFO_2/TaO_x/TiN artificial synaptic device. Nanomaterials 10:2159. https://doi.org/10.3390/nano1011215
6. Park M, Kang M, Kim S (2021) Pulse frequency dependent synaptic characteristics in Ta/SiN/Si memristor device for neuromorphic system. J Alloys Compd 882:160760. https://doi.org/10.1016/j.jallcom.2021.160760
7. Ryu JH, Mahata C, Kim S (2021) Long-term and short-term plasticity of Ta_2O_5/HfO_2 memristor for hardware neuromorphic application. J Alloys Compd. https://doi.org/10.1016/j.jallcom.2020.156675
8. Kim D, Kim S, Kim S (2021) Logic-in-memory application of CMOS compatible silicon nitride memristor. Chaos Solitons Fract 153:11154. https://doi.org/10.1016/j.chaos.2021.111540
9. Lin KL, Hou TH, Shieh J et al (2011) Electrode dependence of filament formation in HfO_2 resistive-switching memory. J Appl Phys 109:084104. https://doi.org/10.1063/1.3567915
10. Rodriguez-Fernandez A, Aldana S, Campabadal F et al (2017) Resistive switching with self-rectifying tunability and influence of the oxide layer thickness in Ni/HfO_2/n^+-Si RRAM devices. IEEE Trans Electron Devices 64:3159–3166. https://doi.org/10.1109/TED.2017.2717497
11. Hu G, An H, Xi J et al (2021) A ZnO micro/nanowire-based photonic synapse with piezo-phototronic modulation. Nano Energy 89:106282. https://doi.org/10.1016/j.nanoen.2021.106282
12. Khan SA, Lee GH, Mahata C et al (2021) Bipolar and complementary resistive switching characteristics and neuromorphic system simulation in a Pt/ZnO/TiN synaptic device. Nanomaterials 11:315. https://doi.org/10.3390/nano11020315
13. Sun J, Tan JB, Chen T (2020) Investigation of electrical noise signal triggered resistive switching and its implications. IEEE Trans Electron Devices 67:4178–4184. https://doi.org/10.1109/TED.2020.3014841
14. Shin J, Kang M, Kim S (2021) Gradual conductance modulation of Ti/WO_x/Pt memristor with self-rectification for a neuromorphic system. Appl Phys Lett 119:012102. https://doi.org/10.1063/5.0053478
15. Chen ZX, Fang Z, Wang Y et al (2014) Impact of Ni concentration on the performance of Ni silicide/HfO_2/TiN resistive RAM (RRAM) cells. J Electron Mater 43:4193–4198. https://doi.org/10.1007/s11664-014-3309-9
16. Luo Q, Xu X, Gong T et al (2018) 8-Layers 3D vertical RRAM with excellent scalability towards storage class memory applications. In: Technical digest—international electron devices meeting, IEDM
17. Yu S, Chen HY, Gao B et al (2013) HfO_x-based vertical resistive switching random access memory suitable for bit-cost-effective three-dimensional cross-point architecture. ACS Nano 7:2320–2325. https://doi.org/10.1021/nn305510u
18. Al-Haddad A, Wang C, Qi H et al (2016) Highly-ordered 3D vertical resistive switching memory arrays with ultralow power consumption and

ultrahigh density. ACS Appl Mater Interfaces 8:23348–23355. https://doi.org/10.1021/acsami.6b05424
19. Yu M, Cai Y, Wang Z et al (2016) Novel vertical 3D structure of TaO_x-based RRAM with self-localized switching region by sidewall electrode oxidation. Sci Rep 6:1–10. https://doi.org/10.1038/srep21020
20. Jeong DS, Thomas R, Katiyar RS et al (2012) Emerging memories: resistive switching mechanisms and current status. Rep Prog Phys 75:076502
21. Lanza M, Wong HSP, Pop E et al (2019) Recommended methods to study resistive switching devices. Adv Electron Mater 5:1800143
22. Waser R, Aono M (2007) Nanoionics-based resistive switching memories. Nat Mater 6:833–840. https://doi.org/10.1038/nmat2023
23. Sawa A (2008) Resistive switching in transition metal oxides. Mater Today 11:28–36
24. Yu S (2014) Overview of resistive switching memory (RRAM) switching mechanism and device modeling. In: Proceedings—IEEE international symposium on circuits and systems
25. Li YT, Long SB, Liu Q et al (2011) An overview of resistive random access memory devices. Chin Sci Bull 56:3072–3078
26. Choi J, Kim S (2020) Improved stability and controllability in ZrN-based resistive memory device by inserting TiO_2 layer. Micromachines 11:905. https://doi.org/10.3390/mi11100905
27. Kim S, Chen J, Chen YC et al (2019) Neuronal dynamics in HfO_x/AlO_y-based homeothermic synaptic memristors with low-power and homogeneous resistive switching. Nanoscale 11:237–245. https://doi.org/10.1039/c8nr06694a
28. Zhang K, Sun K, Wang F et al (2015) Ultra-low power Ni/HfO_2/TiO_x/TiN resistive random access memory with sub-30-nA reset current. IEEE Electron Device Lett 36:1018–1020. https://doi.org/10.1109/LED.2015.2464239
29. Sun QQ, Gu JJ, Chen L et al (2011) Controllable filament with electric field engineering for resistive switching uniformity. IEEE Electron Device Lett 32:1167–1169. https://doi.org/10.1109/LED.2011.2159770
30. Kwon O, Kim Y, Kang M, Kim S (2021) Comparison of synaptic properties considering dopant concentration and device operation polarity in Cu/SiN/SiO_2/p-Si devices for neuromorphic system. Appl Surf Sci 563:150101. https://doi.org/10.1016/j.apsusc.2021.150101
31. Vishwanath SK, Woo H, Jeon S (2018) Enhancement of resistive switching properties in Al_2O_3 bilayer-based atomic switches: Multilevel resistive switching. Nanotechnology 29:235202. https://doi.org/10.1088/1361-6528/aab6a3
32. Chen L, Gou HY, Sun QQ et al (2011) Enhancement of resistive switching characteristics in Al_2O_3-based RRAM with embedded ruthenium nanocrystals. IEEE Electron Device Lett 32:794–796. https://doi.org/10.1109/LED.2011.2125774
33. Chen L, Xu Y, Sun QQ et al (2010) Highly uniform bipolar resistive switching with Al_2O_3 buffer layer in robust NbAlO-based RRAM. IEEE Electron Device Lett 31:356–358. https://doi.org/10.1109/LED.2010.2041183
34. Kim S, Park BG (2016) Nonlinear and multilevel resistive switching memory in Ni/Si_3N_4/Al_2O_3/TiN structures. Appl Phys Lett 108:212103. https://doi.org/10.1063/1.4952719
35. Chen C, Pan F, Wang ZS et al (2012) Bipolar resistive switching with self-rectifying effects in Al/ZnO/Si structure. J Appl Phys 111:013702. https://doi.org/10.1063/1.3672811
36. Wang Z, Yaegashi O, Sakaue H et al (2003) Suppression of native oxide growth in sputtered TaN films and its application to Cu electroless plating. J Appl Phys 94:4697–4701. https://doi.org/10.1063/1.1609644
37. Zhou Q, Zhai J (2014) Study of the bipolar resistive-switching behaviors in Pt/GdO_x/TaN_x structure for RRAM application. Physica Status Solidi A Appl Mater Sci 211:173–179. https://doi.org/10.1002/pssa.201330098
38. Zhou P, Yin M, Wan HJ et al (2009) Role of TaON interface for Cu_xO resistive switching memory based on a combined model. Appl Phys Lett 94:053510. https://doi.org/10.1063/1.3078824
39. Fang R-C, Sun Q-Q, Zhou P et al (2013) High-performance bilayer flexible resistive random access memory based on low-temperature thermal atomic layer deposition. Nanoscale Res Lett 8:1–7. https://doi.org/10.1186/1556-276x-8-92
40. Zhou J, dan Nie D, Jin XB, Xiao W (2020) Controllable nitridation of Ta_2O_5 in molten salts for enhanced photocatalysis. Int J Miner Metall Mater 27:1703–1710. https://doi.org/10.1007/s12613-020-2050-z
41. Misha SH, Tamanna N, Woo J et al (2015) Effect of nitrogen doping on variability of TaO_x-RRAM for low-power 3-bit MLC applications. ECS Solid State Lett 4:P25–P28. https://doi.org/10.1149/2.0011504ssl
42. Cristea D, Cunha L, Gabor C et al (2019) Tantalum oxynitride thin films: assessment of the photocatalytic efficiency and antimicrobial capacity. Nanomaterials 9:476. https://doi.org/10.3390/nano9030476
43. Ismail M, Mahata C, Kim S (2022) Forming-free Pt/Al_2O_3/HfO_2/$HfAlO_x$/TiN memristor with controllable multilevel resistive switching and neuromorphic characteristics for artificial synapse. J Alloys Compd 892:162141. https://doi.org/10.1016/j.jallcom.2021.162141
44. Ryu H, Kim S (2021) Gradually modified conductance in the self-compliance region of an atomic-layer-deposited Pt/TiO_2/$HfAlO_x$/TiN rram device. Metals 11:1199. https://doi.org/10.3390/met11081199
45. Chen MC, Chang TC, Chiu YC et al (2013) The resistive switching characteristics in TaON films for nonvolatile memory applications. Thin Solid Films 528:224–228. https://doi.org/10.1016/j.tsf.2012.09.081
46. Ismail M, Abbas H, Mahata C et al (2022) Optimizing the thickness of Ta_2O_5 interfacial barrier layer to limit the oxidization of Ta ohmic interface and ZrO_2 switching layer for multilevel data storage. J Mater Sci Technol 106:98–107. https://doi.org/10.1016/j.jmst.2021.08.012
47. Lin J, Wang S, Liu H (2021) Multi-level switching of al-doped HfO_2 RRAM with a single voltage amplitude set pulse. Electronics (Switzerland) 10:731. https://doi.org/10.3390/electronics10060731
48. Wu J, Ye C, Zhang J et al (2016) Multilevel characteristics for bipolar resistive random access memory based on hafnium doped SiO_2 switching layer. Mater Sci Semicond Process 43:144–148. https://doi.org/10.1016/j.mssp.2015.12.012
49. Li Y, Long S, Liu Y et al (2015) Conductance quantization in resistive random access memory. Nanoscale Res Lett 10:1–30
50. Celano U, Goux L, Belmonte A et al (2015) Understanding the dual nature of the filament dissolution in conductive bridging devices. J Phys Chem Lett 6:1919–1924. https://doi.org/10.1021/acs.jpclett.5b00633
51. Sharath SU, Vogel S, Molina-Luna L et al (2017) Control of switching modes and conductance quantization in oxygen engineered HfO_x based memristive devices. Adv Funct Mater 27:1700432. https://doi.org/10.1002/adfm.201700432
52. Park J, Lee S, Lee K, Kim S (2021) Conductance quantization behavior in pt/sin/tan rram device for multilevel cell. Metals 11:1918. https://doi.org/10.3390/met11121918
53. Sun Y, Wen D (2018) Conductance quantization in nonvolatile resistive switching memory based on the polymer composite of zinc oxide nanoparticles. J Phys Chem C 122:10582–10591. https://doi.org/10.1021/acs.jpcc.8b01120
54. Gao S, Zeng F, Chen C et al (2013) Conductance quantization in a Ag filament-based polymer resistive memory. Nanotechnology 24:335201. https://doi.org/10.1088/0957-4484/24/33/335201
55. Zhu X, Su W, Liu Y et al (2012) Observation of conductance quantization in oxide-based resistive switching memory. Adv Mater 24:3941–3946. https://doi.org/10.1002/adma.201201506
56. Mehonic A, Vrajitoarea A, Cueff S et al (2013) Quantum conductance in silicon oxide resistive memory devices. Sci Rep 3:1–8. https://doi.org/10.1038/srep02708
57. Gao S, Chen C, Zhai Z et al (2014) Resistive switching and conductance quantization in Ag/SiO_2/indium tin oxide resistive memories. Appl Phys Lett 105:063504. https://doi.org/10.1063/1.4893277
58. Long S, Lian X, Cagli C et al (2013) Quantum-size effects in hafnium-oxide resistive switching. Appl Phys Lett 102:183505. https://doi.org/10.1063/1.4802265
59. Tsuruoka T, Hasegawa T, Terabe K, Aono M (2012) Conductance quantization and synaptic behavior in a Ta_2O_5-based atomic switch. Nanotechnology 23:435705. https://doi.org/10.1088/0957-4484/23/43/435705
60. Chen C, Gao S, Zeng F et al (2013) Conductance quantization in oxygen-anion-migration-based resistive switching memory devices. Appl Phys Lett 103:043510. https://doi.org/10.1063/1.4816747
61. Lv H, Xu X, Sun P et al (2015) Atomic view of filament growth in electrochemical memristive elements. Sci Rep 5:1–8. https://doi.org/10.1038/srep13311
62. Milano G, Aono M, Boarino L et al (2022) Quantum conductance in memristive devices: fundamentals, developments, and applications. Adv Mater. https://doi.org/10.1002/adma.202201248

63. Zhao X, Xu J, Xie D et al (2021) Natural acidic polysaccharide-based memristors for transient electronics: highly controllable quantized conductance for integrated memory and nonvolatile logic applications. Adv Mater 33:1–10. https://doi.org/10.1002/adma.202104023
64. Banerjee W, Hwang H (2019) Quantized conduction device with 6-bit storage based on electrically controllable break junctions. Adv Electron Mater 5:1–10. https://doi.org/10.1002/aelm.201900744
65. Strukov DB, Kohlstedt H (2012) Resistive switching phenomena in thin films: Materials, devices, and applications. MRS Bull 37:108–114
66. Zhang SR, Zhou L, Mao JY et al (2019) Artificial synapse emulated by charge trapping-based resistive switching device. Adv Mater Technol 4:1800342. https://doi.org/10.1002/admt.201800342
67. Rahmani MK, Ismail M, Mahata C, Kim S (2020) Effect of interlayer on resistive switching properties of SnO_2-based memristor for synaptic application. Results Phys 18:103325. https://doi.org/10.1016/j.rinp.2020.103325
68. Park J, Ryu H, Kim S (2021) Nonideal resistive and synaptic characteristics in Ag/ZnO/TiN device for neuromorphic system. Sci Rep 11:1–7. https://doi.org/10.1038/s41598-021-96197-8
69. Cho H, Kim S (2020) Enhancing short-term plasticity by inserting a thin TiO_2 layer in WO_x-based resistive switching memory. Coatings 10:908. https://doi.org/10.3390/COATINGS10090908
70. Ismail M, Mahata C, Kwon O, Kim S (2022) Neuromorphic synapses with high switching uniformity and multilevel memory storage enabled through a Hf-Al-O alloy for artificial intelligence. ACS Appl Electron Mater. https://doi.org/10.1021/acsaelm.2c00023
71. Lee Y, Mahata C, Kang M, Kim S (2021) Short-term and long-term synaptic plasticity in Ag/HfO_2/SiO_2/Si stack by controlling conducting filament strength. Appl Surf Sci 565:150563. https://doi.org/10.1016/j.apsusc.2021.150563
72. Feng G, Jiang J, Zhao Y et al (2020) A sub-10 nm vertical organic/inorganic hybrid transistor for pain-perceptual and sensitization-regulated nociceptor emulation. Adv Mater 32:1–11. https://doi.org/10.1002/adma.201906171
73. Li Y, Yin K, Diao Y et al (2022) A biopolymer-gated ionotronic junctionless oxide transistor array for spatiotemporal pain-perception emulation in nociceptor network. Nanoscale 14:2316–2326. https://doi.org/10.1039/d1nr07896h
74. Jiang J, Hu W, Xie D et al (2019) 2D electric-double-layer phototransistor for photoelectronic and spatiotemporal hybrid neuromorphic integration. Nanoscale 11:1360–1369. https://doi.org/10.1039/c8nr07133k
75. Shen Z, Zhao C, Qi Y et al (2020) Advances of RRAM devices: Resistive switching mechanisms, materials and bionic synaptic application. Nanomaterials 10:1437
76. Lu K, Li Y, He WF et al (2018) Diverse spike-timing-dependent plasticity based on multilevel HfOx memristor for neuromorphic computing. Appl Phys A Mater Sci Process 124:1–9. https://doi.org/10.1007/s00339-018-1847-3

Publisher's Note

Springer Nature remains neutral with regard to jurisdictional claims in published maps and institutional affiliations.